Available online at www.sciencedirect.com
ScienceDirect
Trans. Nonferrous Met. Soc. China 34(2024) 3400−3411
Transactions of Nonferrous Metals Society of China
www.tnmsc.cn

Calcium titanate corrosion inhibitor enabling carbon as inert anode for oxygen evolution in molten chlorides

Kai-fa DU[1,2], Wen-miao LI[1,2], Pei-lin WANG[1,2], Lei GUO[1,2], Di CHEN[1,2], Yong-song MA[1,2], Rui YU[1,2], Hua-yi YIN[1,2], Di-hua WANG[1,2]

1. School of Resource and Environmental Sciences, Wuhan University, Wuhan 430072, China;
2. Hubei International Scientific and Technological Cooperation Base of Sustainable Resources and Energy, Wuhan 430072, China

Received 10 April 2023; accepted 17 April 2024

Abstract: The corrosion inhibition efficacy of titanate ($CaTiO_3$) for carbon anodes in molten salts was investigated through various analytical techniques, including linear sweep voltammetry, X-ray diffraction, scanning electron microscopy, and energy dispersion spectroscopy. The results demonstrate that the addition of $CaTiO_3$ corrosion inhibitor efficiently passivates the carbon anode and leads to the formation of a dense $CaTiO_3$ layer during the electrolysis process in molten $CaCl_2$−CaO. Subsequently, the passivated carbon anode effectively undergoes the oxygen evolution reaction, with an optimal current density for passivation identified at 400 mA/cm^2. Comprehensive investigations, including $CaTiO_3$ solubility tests in molten $CaCl_2$−CaO and numerical modeling of the stability of complex ionic structures, provide compelling evidence supporting "complexation−precipitation" passivation mechanism. This mechanism involves the initial formation of a complex containing $TiO_2{\cdot}n$CaO by $CaTiO_3$ and CaO, which subsequently decomposes to yield $CaTiO_3$, firmly coating the surface of the carbon anode. In practical applications, the integration of $CaTiO_3$ corrosion inhibitor with the carbon anode leads to the successful preparation of the FeCoNiCrMn high-entropy alloy without carbon contamination in the molten $CaCl_2$−CaO.

Key words: corrosion inhibitor; calcium titanate; carbon anode; oxygen evolution reaction

1 Introduction

Molten salt electrolyzers play a pivotal role in facilitating green electrometallurgy for metals such as Al, Ti, Zr, Hf, Nb, Ta, Mo, W, Cr, and their alloys, thanks to their favorable kinetics [1−3]. Typically, carbon anodes are widely utilized in molten halide electrolyzers for metal extraction due to their excellent conductivity [4−6]. However, carbon anodes are frequently subject to heavy consumption by oxygen ions (O^{2-}) generated during the reduction of metal oxides on the cathode [6−8]. This results in the release of a significant amount of CO_2 and CO, leading to severe environmental challenges [9−11]. Notably, the Hall−Héroult process consumes a substantial mass of carbon anodes amounting to 27 million tonnes, accounting for 14% of the total production cost of primary aluminum and generating over 78 million tonnes of CO_2 annually [12−14]. Furthermore, the produced CO_2 can react with O^{2-} to form CO_3^{2-}, which can be electrochemically reduced to carbon on the cathode, thereby reducing the current efficiency of process and contaminating cathodic products [15−17]. Consequently, there is a pressing need for low-cost inert oxygen evolution anodes in molten salt electrolyzers [18−20]. However, due to the highly

Corresponding author: Di-hua WANG, Tel: +86-27-68774216, E-mail: wangdh@whu.edu.cn
DOI: 10.1016/S1003-6326(24)66616-1

corrosive nature of high-temperature molten halides, materials capable of withstanding such harsh working conditions and meeting the requirements of an inert anode are exceedingly rare [21−23]. Thus, consumable carbon anodes, such as graphite and artificial graphite, remain indispensable in industrial molten salt electrolyzers.

In recent years, corrosion inhibition methods aiming at reducing the consumption of carbon anodes have gained significant attention. It has been observed that the oxidation resistance of carbon anodes can be substantially enhanced by optimizing precursor composition and preparation parameters of carbon anodes [24−26]. KHAJI and QASSEMI [10] conducted a study exploring the relationship between manufacturing parameters and carbon anode consumption, revealing that carbon anodes with higher pitch content exhibited superior CO_2 oxidation resistance and lower anode dust resulting from oxidation reactions, which is advantageous for reducing net carbon consumption. Furthermore, anti-oxidation coatings have proven to be a practical approach in protecting carbon anodes within the electrolysis cell [9,27]. WENG et al [28] reported that carbon contamination in cathode products decreased from 2.47 wt.% to 0.57 wt.% when a porous MgO shroud was added to the graphite anode. Most previous research has been focused on reducing excessive carbon anode consumption, including air oxidation, the Boudouard reaction, and carbon dust generation, which contribute to approximately 15% of the total carbon anode consumption [27]. However, the main consumption of carbon anode is generated from the anodic oxidation of carbon ($C+2O^{2-}-4e=CO_2$). Therefore, further efforts should be directed towards investigating whether the carbon anode can function as an inert anode enabling oxygen evolution instead of being consumed through anodic oxidation. This prospect holds great potential for resolving the primary issue associated with carbon anodes.

Drawing insights from corrosion science in room-temperature aqueous solutions [29,30], we apply the idea of using a corrosion inhibitor to stabilize the carbon anode. This study introduces a titanate corrosion inhibitor capable of passivating the graphite anode and facilitating the formation of a protective oxide film on the carbon anode. As a consequence, this passivation process leads to a transformation of the anodic reaction from CO_2 generation to oxygen evolution in the molten $CaCl_2$−CaO. The structure and constitutions of the oxide films formed on the graphite anodes were thoroughly investigated. Moreover, we explored the influence of the basicity of molten salts on the solubility of calcium titanate and utilized density functional theory (DFT) calculations to elucidate the passivation mechanism of the carbon anode. Furthermore, FeCoNiCrMn high-entropy alloy, possessing the advantages of good mechanical properties and corrosion resistance [31], has been successfully synthesized by molten salt electrolysis in previous research [32]. However, carbon contamination of the FeCoNiCrMn alloy was observed when utilizing consumed graphite. To address this issue, in the present work, we prepared the FeCoNiCrMn high-entropy alloy without carbon contamination by employing a carbon anode in molten salts with the incorporation of a titanate corrosion inhibitor. This novel approach allows us to attain the desired properties of high-entropy alloy while mitigating carbon contamination concerns effectively.

2 Experimental

2.1 Electrochemical tests

A Ni crucible with an outer diameter of 12 cm was utilized to contain 1000 g of anhydrous $CaCl_2$, serving as the molten salt bath. The mixed salt was dried at 200 °C for 24 h and then melted at 850 °C in an argon atmosphere. CaO was subjected to heating in air at 1000 °C for 4 h to remove impurities like $Ca(OH)_2$ and $CaCO_3$. Subsequently, CaO and $CaTiO_3$, with concentrations of 2.0 and 0.8 wt.% respectively, were added to the molten $CaCl_2$. All reagents used were of analytical purity and obtained from Sinopharm Chemical Regent Co. Ltd., China. For the anodic polarization experiments, a three-electrode system was employed, and the anodic sweep rate was set at 5 mV/s using an electrochemical workstation (CHI−1140, CH Instrument Co. Ltd., China). A graphite rod with a diameter of 3 mm served as the working electrode, while the counter electrode consisted of NiO powder at the bottom of the Ni crucible. A nickel wire with a diameter of 1 mm, covered with a layer of NiO, served as the reference electrode. Galvanostatic electrolysis was performed

on a carbon anode with a diameter of 10 mm for 1 h, with anodic current densities of 200, 375, 400, and 600 mA/cm^2, respectively. During the experiments, the anodic gas was collected using an alumina tube and analyzed in situ using a gas analyzer (Fig. 1, AGA1000, Aut. EQ. Co. Ltd., China, Precision: 0.1 vol.%). The flow rate of argon gas used was maintained at 60 mL/min.

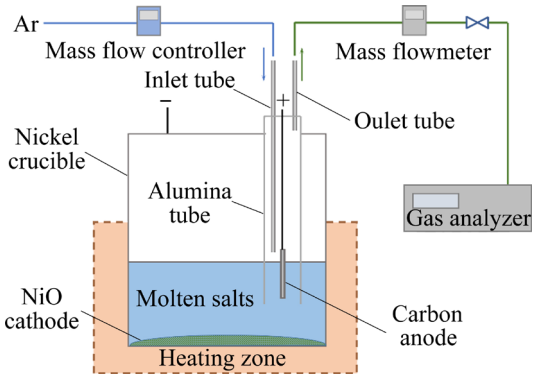

Fig. 1 Schematic of anodic gas analysis equipment

2.2 Preparation of FeCoNiCrMn alloy

The Fe_2O_3, Co_3O_4, NiO, Cr_2O_3 and MnO_2 powders with analytical purity from Sinopharm Chemical Regent Co. Ltd., China, were mixed in a molar ratio of Fe:Co:Ni:Cr:Mn=1:1:1:1:1. The mixture was then die-pressed into cylindrical pellets with a diameter of 20 mm and sintered at 1123 K for 2 h to enhance their mechanical strength. For the electrolysis process, a carbon anode was in-situ pre-passivated for 1 h and used as the anode. The electrolysis was conducted using an oxide pellet cathode on a nickel foam current collector and the pre-passivated carbon anode in molten $CaCl_2$−2wt.%CaO containing 8 g $CaTiO_3$. The entire process took place at 850 °C for 3 h, utilizing a computer-controlled DC power from Shenzhen Neware Electronic Ltd., China.

2.3 Characterizations

After the experiments, all the samples were washed with deionized water to remove any adhered electrolyte and subsequently dried in a vacuum furnace at 80 °C for 12 h. The dried samples were characterized by a high-magnification optical microscopy ((Keyence VHX-5000), X-ray diffraction (XRD, Shimadzu X-ray 6000 with Cu $K_{\alpha1}$ radiation at λ=1.5405Å), scanning electron microscopy (SEM, TESCAN, Mira3 LMH), and energy dispersion spectroscopy (EDS, Oxford, Aztec Energy X-Max 20).

2.4 Solubility of $CaTiO_3$

The solubilities of $CaTiO_3$ in molten $CaCl_2$ with different concentrations of CaO (0, 1.0, 2.0, and 4.0 mol.%) were investigated. First, 10 g of $CaTiO_3$ was added to 1000 g of pre-treated molten $CaCl_2$. After 4 h immersion, a certain number of liquid salts was taken out by a small alumina crucible and then cooled down in a desiccator. The obtained salts were diluted with deionized water, and the titanium ion concentration was analyzed by inductively coupled plasma optical emission spectrometry (ICP-OES, Agilent 730).

2.5 Density function theory (DFT) calculations

First-principle computations were executed by using the CASTEP DFT code with the exchange-correlation functional of Perdew−Burke−Ernzerhof (PBE) based on generalized gradient approximation (GGA) according to the previous report [33,34]. All the atom positions in the CaO, CaF_2, $CaCl_2$, $CaBr_2$ and CaI_2 were geometrically optimized. The *k*-point sampling consists of 4×4×4 Monkhorst−Pack points for all models. During structure optimization, all energy change criterion was set to be 1×10^{-5} eV, and the atoms were relaxed until the force acting on each atom was less than 0.03 eV/Å, the plane wave cutoff was set to be 540 eV, and the van der Waals correction was considered in the modelling.

3 Results and discussion

3.1 Passivation and oxygen evolution behaviour of carbon anode

The anodic behavior of graphite electrodes was studied in molten $CaCl_2$−2wt.%CaO, both with and without the addition of $CaTiO_3$. Figure 2 shows the anodic polarization curves of graphite electrodes in molten $CaCl_2$−2wt.%CaO. By comparing these curves to the oxygen evolution reaction of a platinum electrode (with an onset potential of 0.9 V vs Ni/NiO) [35,36], three oxidation peaks (a1, a2, and a3) can be observed on the graphite electrode, which is in good agreement with previously reported data [16]. The oxidation peaks correspond the oxidation of the carbon anode of Eq. (1), Eq. (2), and Eq. (3) [37−39]:

$$C+CaO-2e=CO(g)+Ca^{2+} \quad (1)$$

$$C+3CaO-4e=CaCO_3+2Ca^{2+} \quad (2)$$

$$C+2CaO-4e=CO_2+2Ca^{2+} \quad (3)$$

The eighth cycle of the anodic polarization curve of the graphite electrode exhibits a similar behavior to the first polarization cycle (Fig. 2), indicating continuous consumption of the graphite electrode. Galvanostatic electrolysis was performed on the carbon anode at a current of 5 A (375 mA/cm^2) for 60 min. As shown in Fig. 3(a), the anodic potential is approximately 0.89 V (vs Ni/NiO), which is lower than the potential required for oxygen evolution. Furthermore, no oxygen gas can be detected in the outlet gas (Fig. 3(a)). The porous appearance and smaller diameter of the graphite electrode after electrolysis (Fig. 3(b)) reveal that the main anodic reaction occurring on the carbon anode is the consumable dissolution reaction (Fig. 4).

Figure 5 shows the anodic polarization curves of graphite electrode in molten $CaCl_2$−2wt.%CaO with the addition of $CaTiO_3$. The oxidation peak

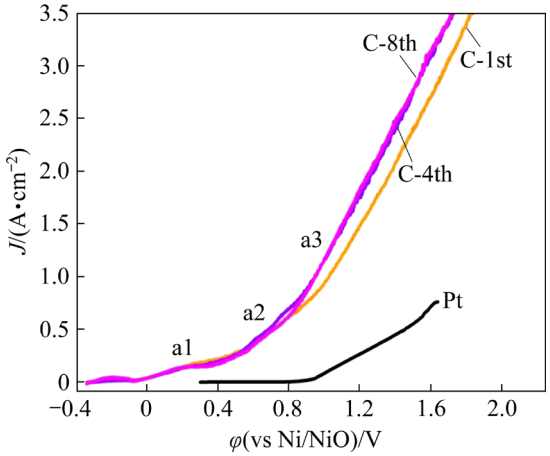

Fig. 2 Anodic polarization curves of carbon electrode in molten $CaCl_2$−2wt.%CaO at 850 °C

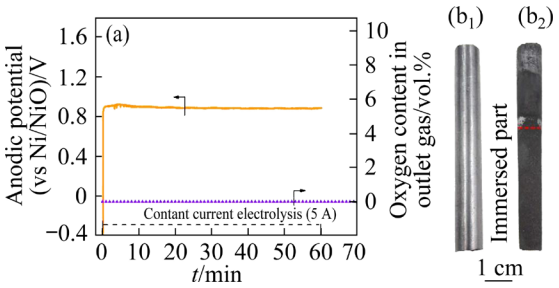

Fig. 3 Plots of anodic potential and oxygen content in outlet gas with time of carbon electrode (a), and photos of graphite electrode before (b_1) and after (b_2) electrolysis in molten $CaCl_2$−2wt.%CaO at 850 °C

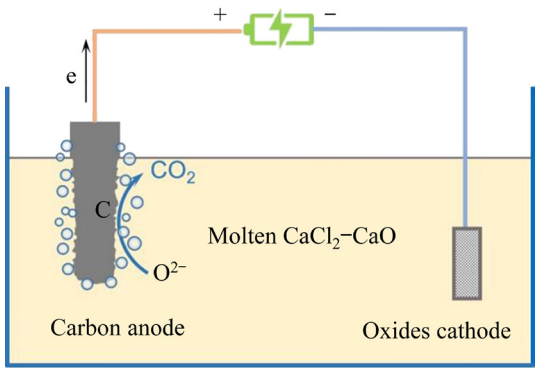

Fig. 4 Schematic illustration of electrolysis cell with carbon anode in molten $CaCl_2$−2wt.%CaO

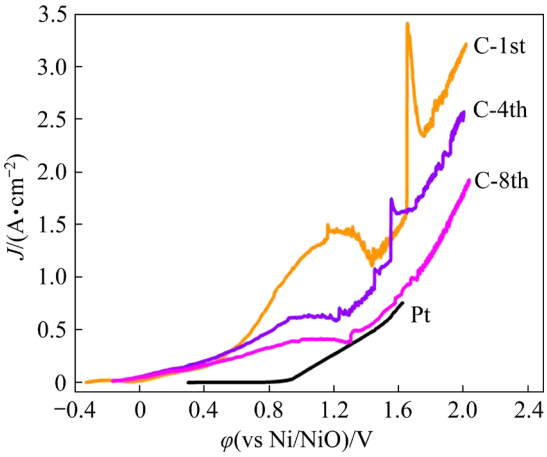

Fig. 5 Anodic polarization curves of carbon electrode in molten $CaCl_2$−2wt.%CaO−0.8wt.%$CaTiO_3$ at 850 °C

located at 1.0 V is associated with the generation of CO_2 (Eq. (3)), and its current density decreases from 1.5 to 0.3 A/cm^2 with increasing anodic polarization cycles, indicating passivation occurring on the carbon anode. The oxygen evolution reaction of the graphite electrode is also observed, with an onset potential at 1.3 V on the anodic polarization curves. In Fig. 6(a), the anodic potential−time plot of the graphite electrode after galvanostatic electrolysis at a current of 5 A is displayed. The chronopotentiometry electrolysis results show that the potential of the carbon anode is ~0.98 V (vs Ni/NiO) at the initial stage and suddenly rises to 1.7 V (vs Ni/NiO) at 18 min. Oxygen is detected at 20 min in the outlet gas, and the oxygen concentration rapidly increases, indicating that the graphite anode is passivated at 18 min, and the anodic reaction is changed from CO/CO_2 generation to oxygen evolution (Fig. 7). After electrolysis in molten salts containing $CaTiO_3$, no noticeable

dimensional change is observed on the carbon anode, and a dense golden-pink coating can be seen on the surface of the graphite electrode (Fig. 6(b)).

The structure and constitution of the surface film on the graphite electrode were further characterized by SEM and XRD. The coating morphology consists of packed cubic particles with diameters of 60−120 μm, as shown in Fig. 8. The cross-section SEM image of the coated graphite electrode indicates that the coating thickness is ~165 μm (Fig. 9). Ti, Ca, and O are homogeneously

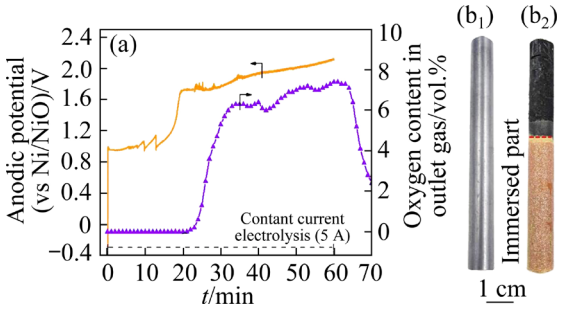

Fig. 6 Plots of anodic potential and oxygen content in outlet gas with time of carbon electrode (a), and photos of graphite electrode before (b_1) and after (b_2) electrolysis in molten $CaCl_2$−2wt.%CaO−0.8wt.% $CaTiO_3$ at 850 °C

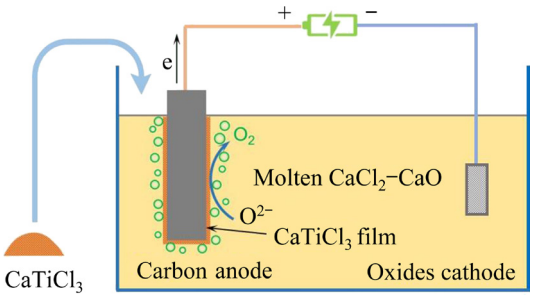

Fig. 7 Schematic illustration of electrolysis cell with graphite anode in molten $CaCl_2$−2wt.%CaO−0.8wt.% $CaTiO_3$

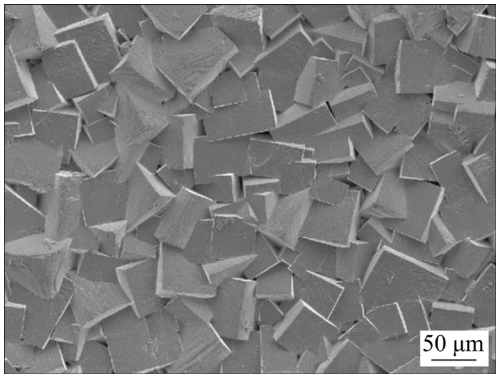

Fig. 8 SEM image of surface oxide film formed on carbon anode after electrolysis in molten $CaCl_2$−2wt.%CaO−0.8wt.%$CaTiO_3$ at 850 °C

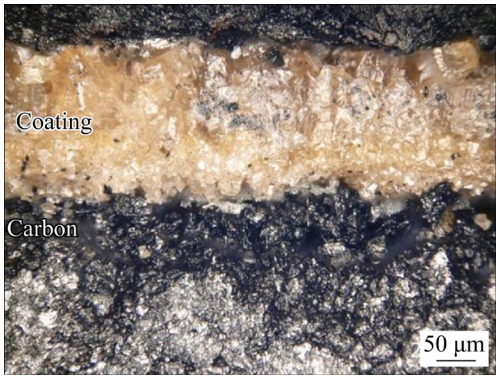

Fig. 9 Micrograph of cross-section of oxide film formed on carbon anode after electrolysis in molten $CaCl_2$−2wt.%CaO−0.8wt.%$CaTiO_3$ at 850 °C

distributed in the coating, as revealed by EDS mappings (Fig. 10). The XRD patterns of the graphite electrode confirm that the coating consists of $CaTiO_3$ (Fig. 11).

3.2 Passivation mechanism of carbon anode

The formation of $CaTiO_3$ coating on the graphite electrode is crucial in converting the consumable carbon anode into an inert oxygen evolution anode, leading to the passivation of the carbon anode. The mechanism of $CaTiO_3$ formation on graphite can be proposed as follows. When $CaTiO_3$ is introduced into CaO-containing $CaCl_2$, it reacts with CaO to form a complex of $TiO_2{\cdot}n$CaO (n>1) or TiO_x^{y-}, as shown in Eq. (4), resulting in a high solubility of $CaTiO_3$ in CaO-containing $CaCl_2$. As depicted in Fig. 12, the solubility of $CaTiO_3$ in molten $CaCl_2$ with different concentrations of CaO is as follows: 475.5 (0 mol.% CaO), 2415.3 (1 mol.% CaO), 3474.5 (2 mol.% CaO), and 5521.5 mg/kg (4 mol.% CaO).

$$CaTiO_3+CaO \rightarrow TiO_2{\cdot}n\text{CaO (dissolved, } n>1) \quad (4)$$

The DFT computational simulation (Fig. 13) provides confirmation that the electron density of the O^{2-} anion in CaO is higher than that of common anion present in the molten salts (such as F^-, Cl^-, Br^-, and I^- in the calcium halide), indicating that O^{2-} can act as a strong complexant in molten salts, favoring the formation of $TiO_2{\cdot}n$CaO when $CaTiO_3$ is added. Moreover, the solubility and dissolution rate of $CaTiO_3$ increase with higher concentration of O^{2-}.

The electrode reaction kinetics suggests that the concentration of O^{2-} near the anode is lower than that in the bulk electrolyte because O^{2-} is

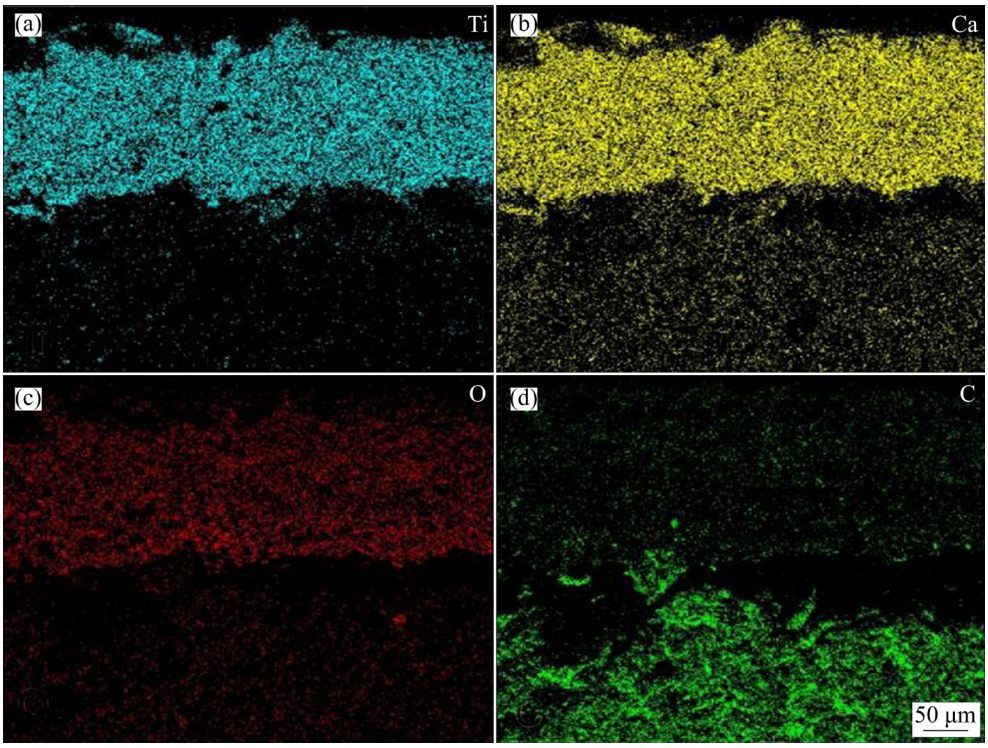

Fig. 10 SEM−EDS mappings of cross-section of oxide film formed on carbon anode after electrolysis in molten $CaCl_2$−2wt.%CaO−0.8wt.%$CaTiO_3$ at 850 °C

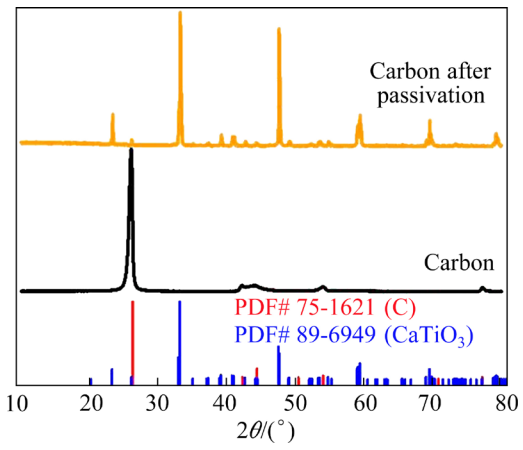

Fig. 11 XRD pattern of oxide film formed on carbon anode after electrolysis in molten $CaCl_2$−2wt.%CaO−0.8wt.%$CaTiO_3$ at 850 °C

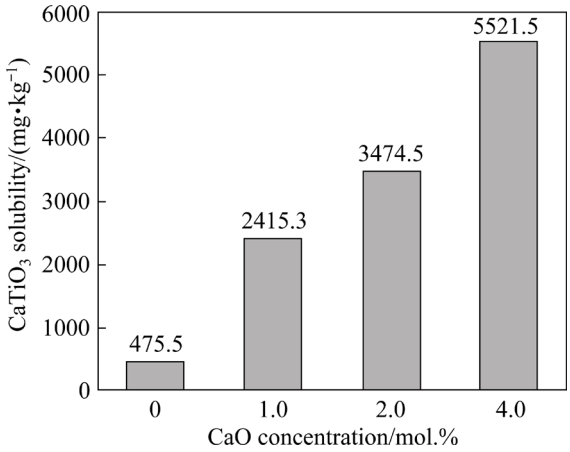

Fig. 12 Solubility of $CaTiO_3$ in molten $CaCl_2$ containing different concentrations of CaO

predominantly consumed by the oxidation of the carbon anode in the diffusion layer (Fig. 14), leading to the creation of an "acidic micro-environment" [40]. In this diffusion layer, the dissolved complex (TiO_2·nCaO) can decompose into $CaTiO_3$ due to the lower O^{2-} concentration (Eq. (5)), subsequently resulting in the precipitation of $CaTiO_3$ on the surface of the graphite electrode and forming a dense protection film.

$$TiO_2 \cdot nCaO\ (\text{dissolved}) \rightarrow CaTiO_3 + CaO \quad (5)$$

Therefore, the passivation mechanism of the carbon anode can be described as "complexation−precipitation" mechanism.

3.3 Effect of current density on passivation of carbon anode

The current density can influence the concentration of O^{2-} near the anode, which significantly impacts the passivation process of the carbon anode. Galvanostatic electrolysis was conducted at different current densities to study

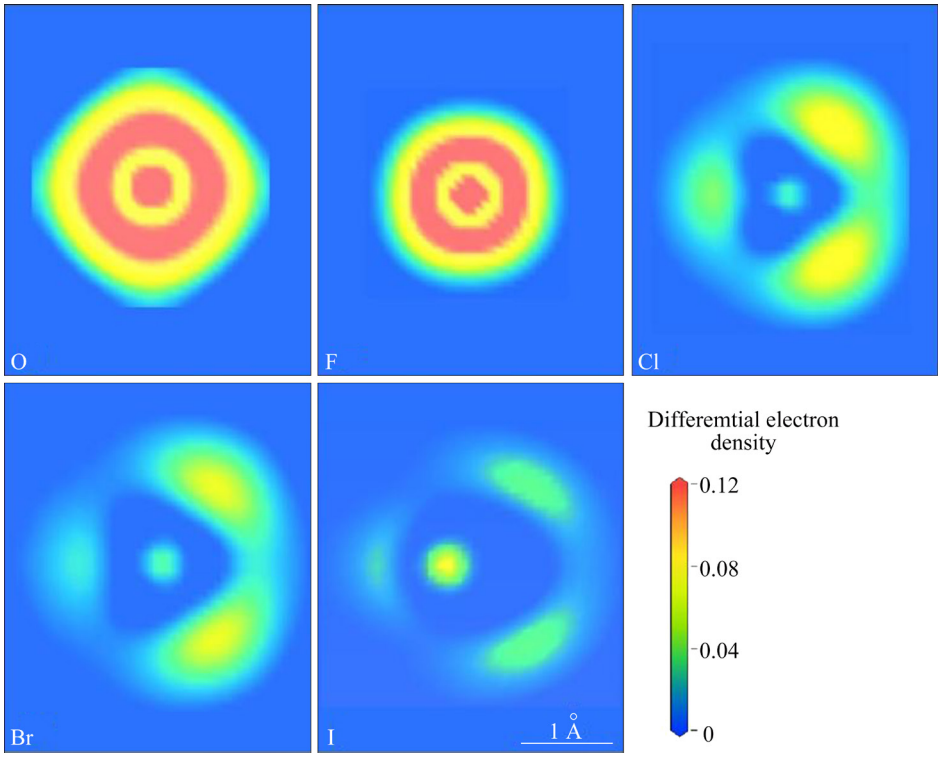

Fig. 13 Differential electron densities of O, F, Cl, Br, and I elements in corresponding calcium salts

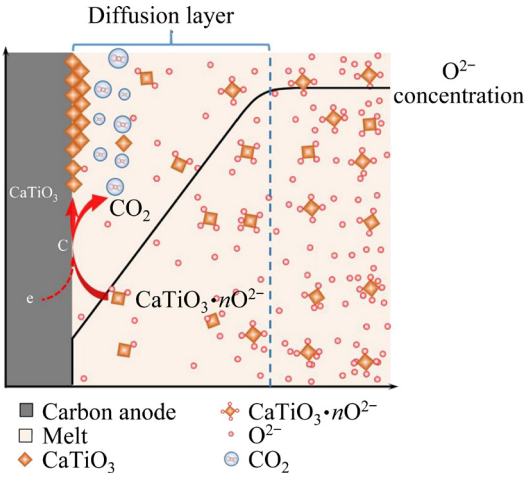

Fig. 14 Schematic illustration of working mechanism of calcium titanate corrosion inhibitor

this effect. After electrolysis, golden coatings are observed on graphite electrodes (Figs. 15(b, e, h)). The anodic potential−time plots obtained under three current densities commonly exhibit two potential stages (Figs. 15(a, d, g)). The first stage represents the oxidation and consumption of the graphite electrode, while the second stage indicates the passivation of the graphite electrode and oxygen evolution. The graphite electrodes are passivated after 27, 12, and 8 min of electrolysis at current densities of 200, 400, and 600 mA/cm^2, respectively (Figs. 15(a, d, g)). At 200 mA/cm^2, the anodic potential fluctuates significantly at the beginning of the passivation stage, possibly due to the simultaneous formation and exfoliation of the in-situ generated passivation film. However, a steady potential of 1.4 V is observed after 40 min, indicating the formation of a stable passivation film with a thickness of around 100 μm (Fig. 15(c)). At 400 and 600 mA/cm^2, the thickness of the passivation film is 140 and 60 μm, respectively (Figs. 15(f, i)). The violent fluctuation in anodic potentials at 600 mA/cm^2 results from the frequent exploration of the passivation film, explaining the smaller thickness of $CaTiO_3$ film obtained at this current density. The higher current density provides a fast formation rate of the passivation film with a large internal stress, while the drastic evolution of oxygen leads to the powerful bubble impacts, causing the frequent exploration of the passivation film. On the other hand, the suitable current density (400 mA/cm^2) results in a relatively stable oxygen evolution potential and the formation of a dense passivation film (Figs. 15(d, e, f)). Overall, the current density plays a crucial role in determining the stability and thickness of the passivation film on the carbon anode during the electrolysis process.

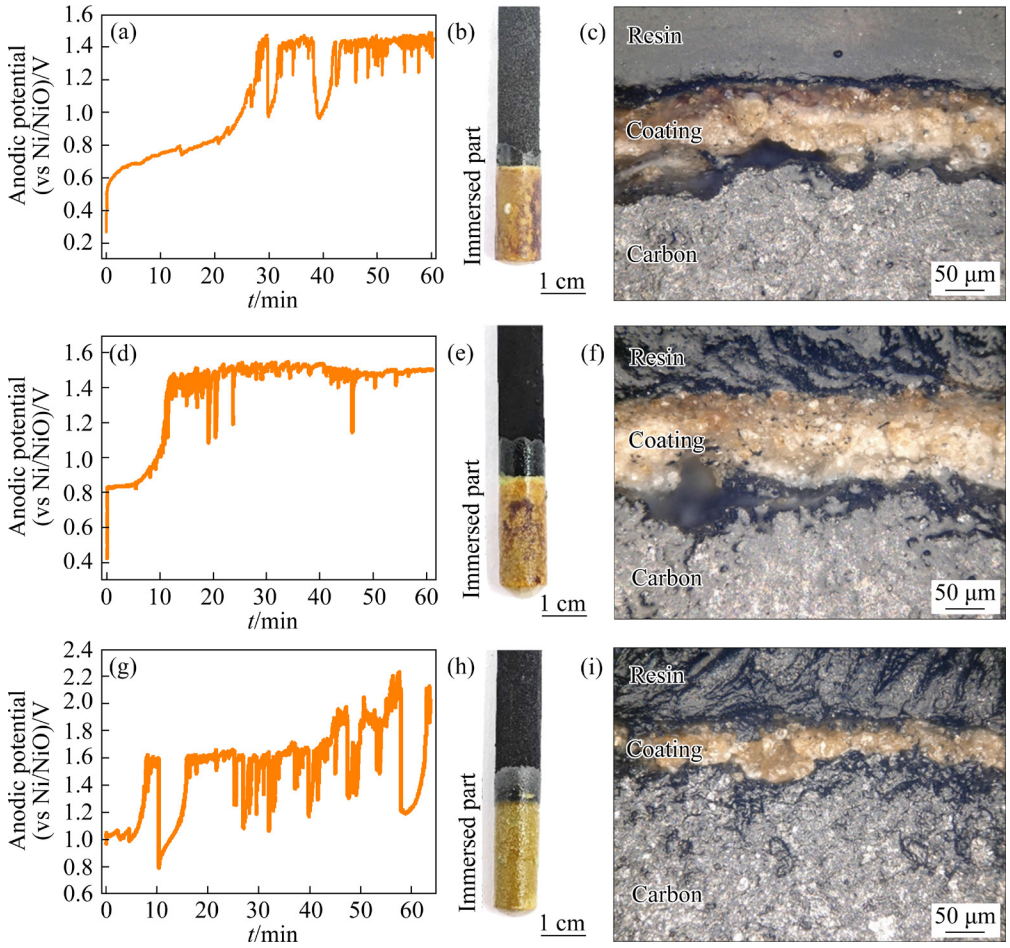

Fig. 15 Variation of anodic potential during constant-current electrolysis (a, d, g), photos after electrolysis (b, e, h) and micrographs of cross-section of carbon anodes (c, f, i) in molten $CaCl_2$−2wt.%CaO−0.8wt.%$CaTiO_3$ at 850 °C and current density of 200 mA/cm^2 (a, b, c), 400 mA/cm^2 (d, e, f), and 600 mA/cm^2 (g, h, i)

3.4 Preparation of FeCoNiCrMn HEA with carbon anode and $CaTiO_3$ corrosion inhibitor

Constant cell voltage electrolysis at 3.0 V was conducted using carbon anodes to prepare FeCoNiCrMn HEA in molten $CaCl_2$−2wt.%CaO, with and without 8 g of $CaTiO_3$ corrosion inhibitor. As shown in Fig. 16, for the electrolysis with $CaTiO_3$ corrosion inhibitor, the current rapidly decreases from 4.5 to 2.5 A within 10 min, and gradually decreases further to 0.6 A in 3 h. In contrast, without the addition of $CaTiO_3$, the current still remains constant at 3.2 A after 3 h (Fig. 16), which can be attributed to the continuous occurrence of the anodic graphite dissolution reaction (Eq. (2)). Simultaneously, the formed $CaCO_3$ is reduced to carbon at the cathode (Eq. (6)):

$$CaCO_3+4e=C+CaO+2O^{2-} \quad (6)$$

The optical images of the oxide pellets before and after electrolysis are shown in Fig. 17(a). With the addition of $CaTiO_3$, the black oxide pellet turns grey with a distinct metallic luster after electrolysis. The XRD and SEM results indicate that the mixed oxides are reduced, and the obtained high-entropy

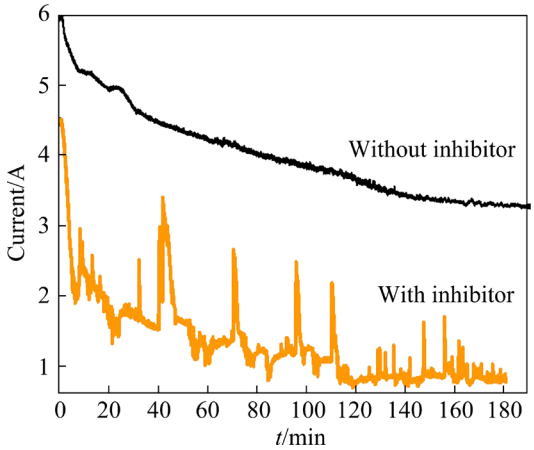

Fig. 16 Variations in current during constant-cell voltage electrolysis with and without $CaTiO_3$ inhibitor in molten $CaCl_2$−2wt.%CaO at 850 °C

alloy displays a single FCC phase with a morphology of approximately 10 μm nodular particles (Figs. 17(b) and 18(a)). Notably, the surface of FeCoNiCrMn nanoparticles appears quite smooth. EDS mapping reveals no presence of carbon particles in the alloy (Fig. 18(b)), indicating that the FeCoNiCrMn HEA is not contaminated by carbon when using the $CaTiO_3$ corrosion inhibitor. Furthermore, the elements of Fe, Co, Ni, Cr, and Mn are uniformly distributed, suggesting that the electrochemical reduction can facilitate the homogenization of the high-entropy alloy.

In contrast, electrolysis without $CaTiO_3$ inhibitor results in a cathodic pellet showing a black-grey color (Fig. 17(a)). Additionally, a weak shoulder peak at ~19° appears in the XRD pattern, commonly associated with amorphous carbon (Fig. 17(b)). SEM images show a wrinkled film covering the nanoparticles (Fig. 19(a)), resulting in a rough surface of FeCoNiCrMn. EDS analysis confirms that the film consists of carbon (Fig. 19(b)). These findings demonstrate that the $CaTiO_3$ corrosion inhibitor effectively prevents carbon contamination of the alloys during the molten salt electrometallurgy process using a carbon anode.

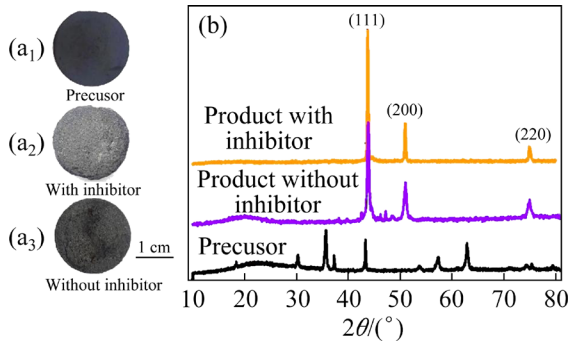

Fig. 17 Photographs of solid oxides cathode before (a_1) and after electrolysis with (a_2) and without (a_3) $CaTiO_3$ inhibitor; XRD patterns of oxide cathode before and after electrolysis in molten $CaCl_2$−2wt.%CaO at 850 °C using carbon anode (b)

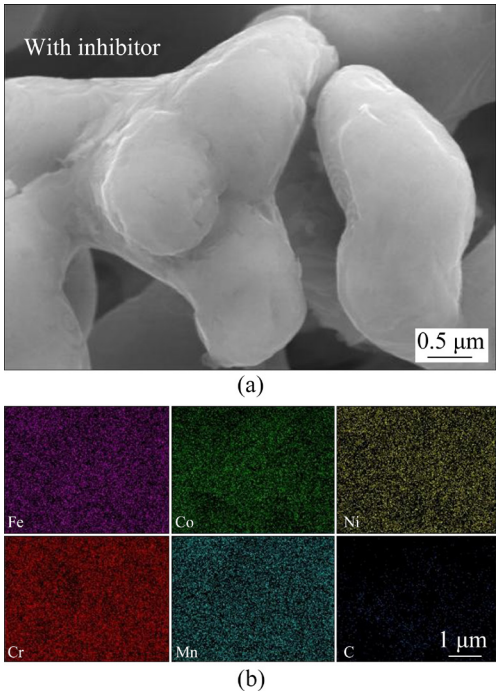

Fig. 18 SEM image (a) and EDS mappings (b) of FeCoNiCrMn alloy obtained in molten $CaCl_2$−2wt.%CaO with addition of 8 g $CaTiO_3$ using carbon anode

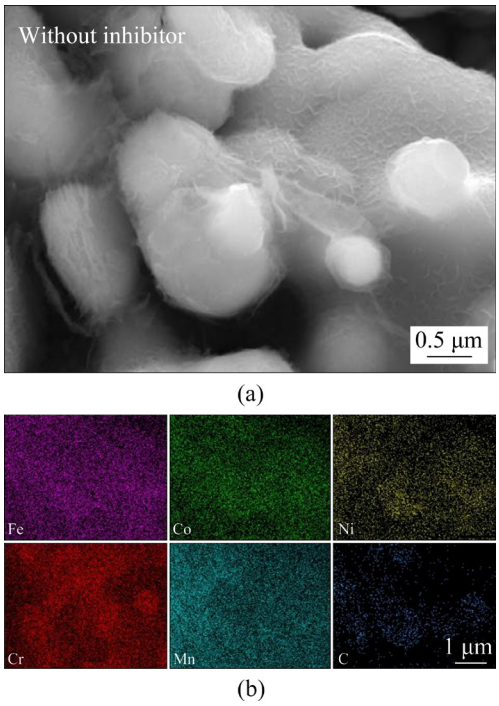

Fig. 19 SEM image (a) and EDS mappings (b) of FeCoNiCrMn alloy obtained in molten $CaCl_2$−2wt.%CaO at 850 °C using carbon anode

4 Conclusions

(1) A titanate corrosion inhibitor was investigated for its ability to stabilize the carbon anode and transform the anodic reaction from CO_2 generation to oxygen evolution. This is achieved by facilitating the formation of a dense $CaTiO_3$ protective film on the carbon anode in molten $CaCl_2$−CaO.

(2) The passivation mechanism of the carbon

anode can be described as the "complexation−precipitation" principle, where a complex of $TiO_2 \cdot nCaO$ is formed and subsequently decomposed to yield $CaTiO_3$ on the carbon anode.

(3) The optimal current density for carbon anode passivation is determined to be 400 mA/cm^2 during electrolysis in molten $CaCl_2$−2wt.%CaO with the addition of 0.8 wt.% $CaTiO_3$ corrosion inhibitor.

(4) By utilizing a carbon anode and $CaTiO_3$ corrosion inhibitor, the FeCoNiCrMn high-entropy alloy is successfully prepared without any carbon contamination.

CRediT authorship contribution statement

Kai-fa DU: Conceptualization, Methodology, Investigation, Writing − Original draft; **Wen-miao LI:** Resources; **Pei-lin WANG:** Validation; **Lei GUO:** Investigation; **Di CHEN:** Data curation; **Yong-song MA:** Formal analysis; **Rui YU:** Writing − Reviewing and editing; **Hua-yi YIN:** Supervision, Writing − Reviewing and editing; **Di-hua WANG:** Conceptualization, Supervision, Writing − Reviewing and editing.

Declaration of competing interest

The authors declare that they have no known competing financial interests or personal relationships that could have appeared to influence the work reported in this paper.

Acknowledgments

This work was supported by the National Natural Science Foundation of China (Nos. 52031008, 51874211, 21673162, 51325102, U22B2071), the International Science and Technology Cooperation Program of China (No. 2015DFA90750), and the China Postdoctoral Science Foundation (No. 2020M682468).

References

[1] ZHOU Xin-yu, DOU Zhi-he, ZHANG Ting-an, YAN Ji-sen, YAN Jian-peng. Preparation of low-oxygen Ti powder from TiO2 through combining self-propagating high temperature synthesis and electrodeoxidation [J]. Transactions of Nonferrous Metals Society of China, 2022, 32(10): 3469−3477. DOI: 10.1016/S1003-6326(22)66033-3.

[2] HARALDSSON J, JOHANSSON M T. Review of measures for improved energy efficiency in production-related processes in the aluminium industry – From electrolysis to recycling [J]. Renewable and Sustainable Energy Reviews, 2018, 93: 525−548. DOI: //doi.org/10.1016/j.rser.2018.05.043.

[3] ALLANORE A, YIN L, SADOWAY D R. A new anode material for oxygen evolution in molten oxide electrolysis [J]. Nature, 2013, 497(7449): 353−356. DOI://doi.org/10.1038/nature12134.

[4] PANG Zhong-ya, LI Xiang, ZHANG Xue-qiang, LI Jin-jian, WANG Shu-juan, XIONG Xiao-lu, LI Guang-shi, XU Qian, ZHOU Zhong-fu, ZOU Xing-li, LU Xiong-gang. Molten salt electrosynthesis of silicon carbide nanoparticles and their photoluminescence property [J]. Transactions of Nonferrous Metals Society of China, 2022, 32(11): 3790−3800. DOI: 10.1016/S1003-6326(22)66058-8.

[5] VISHNU D S M, SURE J, MOHANDAS K S. Corrosion of high density graphite anodes during direct electrochemical de-oxidation of solid oxides in molten $CaCl_2$ medium [J]. Carbon, 2015, 93: 782−792. DOI: 10.1016/j.carbon.2015.05.093.

[6] XIE Hong-wei, ZHAO Hai-jia, SONG Qiu-shi, NING Zhi-qiang, QU Jia-kang, YIN Hua-yi. Anodic gases generated on a carbon electrode in oxide-ion containing molten $CaCl_2$ for the electro-deoxidation process [J]. Journal of the Electrochemical Society, 2018, 165(14): E759−E762. DOI: 10.1149/2.0251814jes.

[7] MA Tong-xiang, LUO Xiang-yu, YANG Yu, HU Mei-long, WEN Liang-ying, ZHANG Sheng-fu, HU Li-wen. Reducing carbon contamination by controlling CO_3^{2-} formation during electrochemical reduction of TiO_2 [J]. Metallurgical and Materials Transactions B, 2021, 52(2): 1061−1070. DOI: 10.1007/s11663-021-02078-w.

[8] LAI Ping-sheng, MA Tong-xiang, HU Mei-long. Effect of wettability between molten salt with graphite anode on the electro-reduction of titanium dioxide [J]. JOM, 2019, 71(3): 1033−1040. DOI: 10.1007/s11837-018-03322-6.

[9] SUN Ke-na, LI Jie, ZHANG Hong-liang, LI Tian-shuang. Microscopic mechanism of perfluorocarbon gas formation in aluminum electrolysis process [J]. Transactions of Nonferrous Metals Society of China, 2022, 32(5): 1705−1717 . DOI: 10.1016/S1003-6326(22)65904-1.

[10] KHAJI K, QASSEMI M A. The role of anode manufacturing processes in net carbon consumption [J]. Metals−Open Access Metallurgy Journal, 2016, 6(6): 128. DOI:10.3390/met6060128.

[11] PADAMATA S K, YASINSKIY A, POLYAKOV P V. Progress of inert anodes in aluminium industry: Review [J]. Journal of Siberian Federal University Chemistry, 2018, 11(1): 18−30. DOI: 10.17516/1998-2836-0055.

[12] SAEVARSDOTTIR G, KVANDE H, WELCH B J. Aluminum production in the times of climate change: The global challenge to reduce the carbon footprint and prevent carbon leakage [J]. JOM, 2020, 72(1): 296−308. DOI: 10.1007/s11837-019-03918-6.

[13] HAARBERG G M, KVALHEIM E, RATVIK A P , XIAO S J, MOKKELBOST T. Depolarised gas anodes for aluminium electrowinning [J]. Transactions of Nonferrous Metals Society of China, 2010, 20(11): 2152−2154. DOI:10.1016/S1003-6326(09)60434-9.

[14] YANG Yi, GUO Yao-qi, ZHU Wen-song, HUANG Jian-bai. Environmental impact assessment of China's primary aluminum based on life cycle assessment [J]. Transactions of Nonferrous Metals Society of China, 2019, 29(8): 1784−1792. DOI: 10.1016/S1003-6326(19)65086-7.

[15] VISHNU S M, SANIL N, PANNEERSELVAM G, SUDHA R, MOHANDAS K S, NAGARAJAN K. Mechanism of direct electrochemical reduction of solid UO_2 to uranium metal in $CaCl_2$−48mol.%NaCl melt [J]. Journal of the Electrochemical Society, 2013, 160(9): D394−D402. DOI: 10.1149/2.080309jes

[16] CHEN Hua-lin, JIN Xian-bo, YU Lin-po, CHEN G Z. Influences of graphite anode area on electrolysis of solid metal oxides in molten salts [J]. Journal of Solid State Electrochemistry, 2014, 18(12): 3317−3325. DOI: 10.1007/s10008-014-2645-2.

[17] FENG Lu-xing, XUE Ji-lai, NDONG G K, LI Xiang, LANG Guang-hui, LIN Ri-fu, LI Wen-xiang, XU Xiu-qin. Effects of current density and temperature on anode carbon consumption in aluminum electrolysis [M]. John Wiley & Sons, Ltd, 2015. DOI:10. 1002/9781119093435.ch194.

[18] GE Jian-bang, ZOU Xing-li, ALMASSI S, JI Li, CHAPLIN B P, BARD A J. Electrochemical production of Si without generation of CO_2 based on the use of a dimensionally stable anode in molten $CaCl_2$ [J]. Angewandte Chemie International Edition, 2019, 58(45): 16223−16228. DOI:10.1002/anie.201905991.

[19] PADAMATA S K, YASINSKIY A, SHABANOV A, BERMESHEV T, YANG Y, WANG Z, CAO D, POLYAKOV P. Improving corrosion resistance of Cu−Al-based anodes in $KF-AlF_3-Al_2O_3$ melts [J]. Transactions of Nonferrous Metals Society of China, 2022, 32(1): 354−363. DOI: 10.1016/ S1003-6326(22)65800-X.

[20] DU Kai-fa, GAO En-lai, ZHANG Chun-bo, MA Yong-song, WANG Pei-lin, YU Rui, LI Wen-miao, ZHENG Kai-yuan, CHENG Xin-hua, TANG Di-yong, DENG Bo-wen, YIN Hua-yi, WANG Di-hua. An iron-base oxygen-evolution electrode for high-temperature electrolyzers [J]. Nature Communications, 2023, 14(1): 253. DOI:10.1038/s41467-023-35904-7.

[21] DU Kai-fa, YU Rui, GAO Mu-xing, CHEN Zhi-gang, MAO Xu-hui, ZHU Hua, WANG Di-hua. Durability of platinum coating anode in molten carbonate electrolysis cell [J]. Corrosion Science, 2019, 153: 12−18. DOI:10.1016/j.corsci.2019.03.028.

[22] ALZAMANI M, JAFARZADEH K, FATTAH-ALHOSSEINI A. Corrosion behavior of Ce-doped Ni−10Cu−11Fe−6Al (wt.%) inert anode in molten $CaCl_2$ salt [J]. Journal of Rare Earths, 2018, 37: 218−224. DOI:10.1016/j.jre.2018.05.016.

[23] HUANG Yi-peng, YANG You-jian, ZHU ling-meng, LIU Feng-guo, WANG Zhao-wen, GAO Bing-liang, SHI Zhong-ning, HU Xian-wei. Electrochemical behavior of Fe−Ni alloys as an inert anode for aluminum electrolysis [J]. International Journal of Electrochemical Science, 2019, 14: 6325−6336. DOI:10.20964/2019.07.42.

[24] WANG Yao-wu, PENG Jian-ping, DI Yue-zhong, FENG Nai-xiang. Production of carbon anodes by high-temperature mould pressing [J]. Transactions of Nonferrous Metals Society of China, 2013, 23(10): 3119−3124. DOI: 10.1016/S1003-6326(13)62842-3.

[25] XIAO Jin, DING Feng-qi, LI Jie, ZOU Zhong, HU Guo-rong, LIU Ye-xiang. Industrial testing of property-modified prebaked carbon anode for aluminum electrolysis [J]. Transactions of Nonferrous Metals Society of China, 2003, 13(3): 686−689. DOI:10.1016/S1359-6462(03)00134-9.

[26] LAI Yan-qing, LI Jie, LI Qing-yu, DING Feng-qi. Effect of aluminum-containing additives on the reactivity in air and CO_2 of carbon anode for aluminum electrolysis [J]. Rare Metals, 2004, 23(2): 109−114. DOI:10.1016/j.cub.2004.05.055.

[27] JASSIM A, JABRI N A, RABBAA S A, MOFOR E G, JAMAL J. Innovative anode coating technology to reduce anode carbon consumption in aluminum electrolysis cells [C]//Light Metals 2019. The Minerals, Metals & Materials Series. Springer, 2019: 745−752. DOI: 10.1007/978-3-030-05864-7_91.

[28] WENG Wei, WANG Ming-yong, GONG Xu-zhong, WANG Zhi, WANG Dong, GUO Zhan-cheng. Mechanism analysis of carbon contamination and the inhibition by an anode structure during soluble K_2CrO_4 electrolysis in $CaCl_2$−KCl molten salt [J]. Journal of the Electrochemical Society, 2017, 164(12): E360−E366. DOI:10.1149/2.1951712jes.

[29] ZHAO Qian, YAN Kai-li, CUI Zhe, WEN Bing-yao, XUE Feng, LI Jin-tong, GUO Jun-nan, XU Ao, QIAO Kai-ming, YE Rong-chang, LONG Yi, ZHANG Da-wei, LUO Hong, TASKAEV S, ZHANG Hu. Data driven accelerated design of high-efficiency corrosion inhibitor for magnetic refrigeration materials [J]. Corrosion Science, 2023, 216: 111115. https://doi.org/10.1016/j.corsci.2023.111115.

[30] REN Chen-hao, MA Ling-wei, LUO Xie-jing, DONG Chao-fang, GUI Tai-jiang, WANG Bo, LI Xiao-gang, ZHANG Da-wei. High-throughput assessment of corrosion inhibitor mixtures on carbon steel via droplet microarray [J]. Corrosion Science, 2023, 213: 110967. DOI: //doi.org/10.1016/j.corsci.2023.110967.

[31] FU Jian-xin, CAO Cheng-ming, TONG Wei, PENG Liang-ming. Effect of thermomechanical processing on microstructure and mechanical properties of CoCrFeNiMn high entropy alloy [J]. Transactions of Nonferrous Metals Society of China, 2018, 28(5): 931−938. DOI: 10.1016/S1003-6326(18)64727-2.

[32] WANG Bin, HUANG Jian, FAN Jin-hang, DOU Yan-peng, ZHU Hua, WANG Di-hua. Preparation of FeCoNiCrMn high entropy alloy by electrochemical reduction of solid oxides in molten salt and its corrosion behavior in aqueous solution [J]. Journal of the Electrochemical Society, 2017, 164(14): E575−E579. DOI:10.1149/2.1521714jes.

[33] PERDEW J P, BURKE K, ERNZERHOF M. Generalized gradient approximation made simple [J]. Physical Review Letters, 1996, 77(18): 3865−3868. DOI:10.1103/PhysRevLett.77.3865.

[34] QIN Jing-jing, CHU Kai-bin, HUANG Yun-peng, ZHU Xiang-miao, HOFKENS J, HE Guan-jie, PARKIN I P, LAI Fei-li, LIU Tian-xi. The bionic sunflower: A bio-inspired autonomous light tracking photocatalytic system [J]. Energy & Environmental Science, 2021, 14(7): 3931−3937. DOI: 10.1039/D1EE00587A.

[35] DU Yang, KOU Ming-yin, TU Ji-guo, WANG Ming-yong, JIAO Shu-qiang. An investigation into the anodic behavior of TiB_2 in a $CaCl_2$-based molten salt [J]. Corrosion Science, 2021, 178: 109089. https://doi.org/10.1016/j.corsci.2020.109089.

[36] TUNOLD R, HAARBERG G M, OSEN K S, MARTINEZ A M, SANDNES E. Anode processes on carbon in chloride−oxide melts [J]. ECS Transactions, 2011, 35(23): 1−9. DOI:10.1149/1.3646097.

[37] MOHAMEDI M. Anodic behavior of carbon electrodes in CaO−$CaCl_2$ Melts at 1123 K [J]. Journal of the Electrochemical Society, 1999, 146(4): 1472−1477. DOI:10.1149/1.1391789.

[38] MATSUURA F, WAKAMATSU T, NATSUI S, KIKUCHI T, SUZUKI R O. CO gas production by molten salt electrolysis from CO_2 gas [J]. ISIJ International, 2015, 55(2): 404−408. DOI: 10.2355/isijinternational.55.404.

[39] LEBEDEV V A, SAL'NIKOV V I, TARABAEV M V, SIZIKOV I A, RYMKEVICH D A. Kinetics and mechanism of the processes occurring at graphite anode in a CaO−$CaCl_2$ melt [J]. Russian Journal of Applied Chemistry, 2007, 80(9): 1498−1502. DOI:10.1134/S107042720709011X.

[40] GAO Mu-xing, DENG Bo-wen, CHEN Zhi-gang, TAO Meng, WANG Di-hua. Cathodic reaction kinetics for CO_2 capture and utilization in molten carbonates at mild temperatures [J]. Electrochemistry Communications, 2018, 88: 79−82. DOI: //doi.org/10.1016/j.elecom.2018.02.003.

高温氯化盐体系中将炭素阳极转变为惰性析氧阳极的钛酸钙缓蚀剂

杜开发[1,2]，李闻淼[1,2]，汪沛霖[1,2]，郭 磊[1,2]，陈 迪[1,2]，
马永松[1,2]，余 锐[1,2]，尹华意[1,2]，汪的华[1,2]

1. 武汉大学 资源与环境科学学院，武汉 430072；
2. 湖北省资源与能源可持续利用技术示范型国际科技合作基地，武汉 430072

摘 要：采用多种分析技术，包括线性扫描伏安法、X 射线衍射、扫描电镜和能量色散光谱，研究 $CaTiO_3$ 缓蚀剂在熔融盐体系中的缓蚀功效。当炭素阳极在添加 $CaTiO_3$ 缓蚀剂的 $CaCl_2$−CaO 电解体系中使用时，表面发生钝化并且生成一层致密的 $CaTiO_3$ 氧化膜。钝化炭素电极发生析氧反应，最佳钝化电流密度为 400 mA/cm^2。通过 $CaTiO_3$ 在 $CaCl_2$−CaO 体系中的溶解度实验及阴离子配合能力模拟计算发现，$CaTiO_3$ 缓蚀剂的钝化机理为“配合溶解−沉淀”，该过程中 $CaTiO_3$ 与 CaO 结合形成 TiO_2·*n*CaO 配合物，随后配合物在炭素阳极表面形成 $CaTiO_3$ 氧化膜。实际应用中可利用炭素阳极和 $CaTiO_3$ 缓蚀剂实现无碳污染 FeCoNiCrMn 高熵合金的成功制备。

关键词：缓蚀剂；钛酸钙；炭素阳极；析氧反应

(Edited by Bing YANG)